Acta Materialia 264 (2024) 119571

Contents lists available at ScienceDirect

Acta Materialia

journal homepage: www.elsevier.com/locate/actamat

Full length article

Revealing 'invisible' subsurface structural change/damage in silicate glass made by 'nearly-elastic contact' with a spherical smooth surface

Yen-Ting Lin [a], Andrew L. Ogrinc [a], Ava N. Zoba [a], Jongcheol Lee [a], Seokhoon Jang [a], Nicholas J. Smith [b], Joy Banerjee [b], Andrew Antony [c], Gabriel Agnello [b], Seong H. Kim [a,*]

[a] Department of Chemical Engineering and Materials Research Institute, The Pennsylvania State University, University Park, PA 16802, USA
[b] Science & Technology Division, Corning Incorporated, Corning, NY 14831, USA
[c] Manufacturing, Technology, and Engineering Division, Corning Incorporated, Corning, NY 14831, USA

ARTICLE INFO

Keywords:
Glass surface
Elastic deformation
Glass corrosion
Mechanical testing

ABSTRACT

This research delves into the hypothesis that elastic contact with an external object can generate `invisible' surface defects, consequently reducing the apparent load to failure, or strength, of glass. This theory, while longstanding, has left the intricate details associated with such defects largely unknown. Utilizing vibrational spectroscopic techniques—with a depth sensitivity on the order of approximately 100 nm—and chemical etching, the study investigates subsurface structural alterations in and around the area subjected to nominally-elastic contact with a Hertzian indenter. Direct contact with the spherical indenter led to the recovery of over 99.96 % of the surface topography, suggesting a near-perfect post-indentation surface. However, surface-sensitive vibrational spectroscopy unveiled structural changes in the subsurface silicate network. Additionally, a shift in the vibrational spectrum was observed in areas that had experienced elastic deformation along with the contact region and fully recovered upon unloading. This shift indicates residual structural changes, even in these non-contacted regions. When the indenter tip was slid across the surface under loads much lower than the nominal yield strength, interfacial friction made the top-most region more susceptible to base-catalyzed hydrolysis. The depth affected by friction was significantly shallower than the length scale of the principal stress fields at maximum load during Hertzian indentation. Despite the glass surface maintaining its microscopic defect-free appearance, these subsurface structural changes—induced by indentation and friction—are proposed to be key factors responsile for the decrease in the apparent load to failure of glass.

1. Introduction

The mechanical and chemical stability as well as optical transparency of silicate glasses make them ideal for use in various industrial and engineering applications such as architectural windows, food containers, display panels [1,2], solar modules [3], and optoelectronics [4,5]. However, physical contacts with foreign materials during storage, transport, installation and usage can introduce defects to the glass surface, which can lead to deterioration in its mechanical strength and chemical durability [6–8]. It was hypothesized that strength weakening and durability reduction originate from a surface damage after contact with foreign objects [9,10]. However, unless they are optically visible, the existence of surface defects has been difficult to verify with direct experimental measurements. Thus, the molecular or structural origin of strength-weakening defects are still incompletely understood.

The difficulty in revealing chemical or structural defects in the 'free-of-any-visible-damage' glass surface and understanding their impacts on mechanical and mechanochemical behaviors originates mainly from the lack of proper characterization techniques to find and analyze such defects [6,7]. Although various spectroscopic and scattering techniques are available to analyze the bulk structure of glass [11–13], they are either incapable of or inefficient at examining localized or heterogeneous surface defects due to the lack of spatial resolution or surface sensitivity that is needed to detect the 'defect' signal without contributions from the 'defect-free' bulk signal [14–17]. Recently, advancements in nano-scale vibrational spectroscopy have enabled the visualization of structural heterogeneity in glass [6,16,18]. These new techniques allow the detection of localized subsurface damage through changes in vibrational spectral features of a glass network.

A recent study that analyzed nanoindentation marks on a silica glass

* Corresponding author.
E-mail address: shk10@psu.edu (S.H. Kim).

https://doi.org/10.1016/j.actamat.2023.119571
Received 9 July 2023; Received in revised form 30 October 2023; Accepted 2 December 2023
Available online 3 December 2023

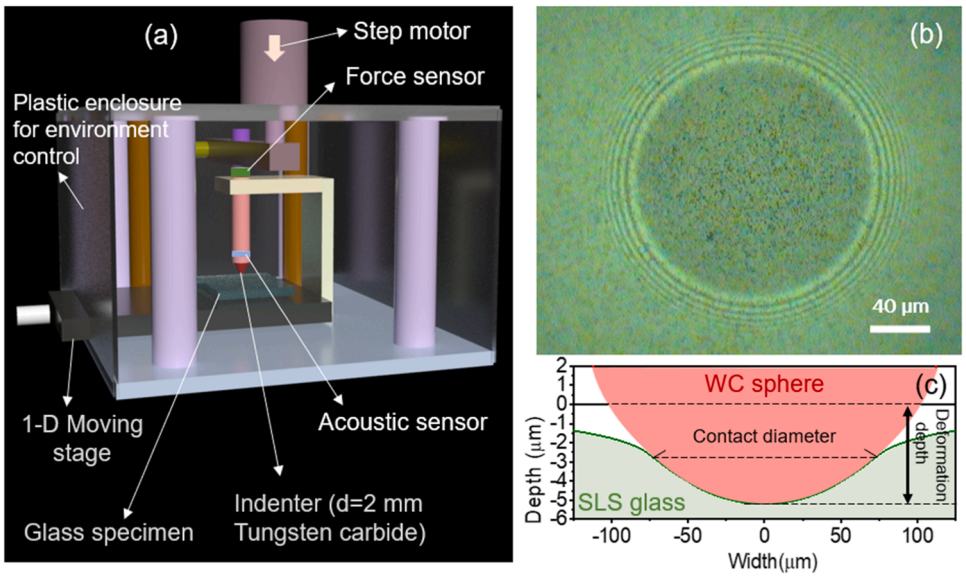

Fig. 1. (a) Hertzian indentation system equipped with acoustic sensor and environmental control. (b) Optical microscope image of the WC ball in contact with the SLS glass at 40 N load taken through the glass with an inverted microscope setup, reproduced with permission from Ref. [28]. Newton's ring fringes in the periphery of the contact area are due to optical interferences between the WC indenter tip and the 'sunk-in' glass surface. (c) Deformation of the SLS surface upon indentation with the WC sphere at 40 N calculated with the Hertzian indentation theory [33]. Note that the calculated contact diameter agrees well with the optical microscope image shown in (b).

with scattering-based nano-scale scanning near-field optical microscopy coupled with Fourier transform infrared spectroscopy (a.k.a. 'nano-FTIR') revealed that, after indentation with a Berkovich tip, the elastically-recovered area around the plastic deformation region had small but measurable changes in vibrational spectral features that could be related to the alteration of the silica network structure [6]. In the periphery region, the indentation stress is low. Thus, the full recovery in topography means that the contact was elastic in that region. The residual structural change observed in the elastic contact region was a surprising discovery. In a single crystalline material, structural change without any volume change is unlikely to occur since the system is in the equilibrium state at a given pressure and temperature. In the case of glass, which is in a non-equilibrium state, its physical properties are path-dependent; in other words, the metastable nature of the amorphous network embraces variances in the local structure which differ depending on the history of thermal or mechanical processing it has experienced. Therefore, structural alteration can occur in the subsurface region after physical contacts with foreign objects even if the glass surface looks nearly defect-free or unaltered topography-wise [7,8].

The previous nano-FTIR study [6] challenged the assumption that the glass network structure will not be altered after contact with a load that is lower than the nominal yielding threshold [19–21]. But, in that study, the subsurface structural modification of the elastic contact region was observed within ~100 nm from the boundary of the nano-indent. Thus, it is still possible that the subsurface region is influenced by plastic deformation although the topmost surface is fully recovered to the initial topography [22].

In this work, we have employed another surface-sensitive IR spectroscopy technique which relies on the atomic force microscopic detection of the photothermal response of materials upon IR absorption (abbreviated as AFM-IR hereafter) [16] in order to probe subsurface structural changes inside and around the surface region after the contact with a tungsten carbide sphere (Hertzian indenter) at loads far below the crack-initiation load (CIL). Instead of fused silica, which is known as an anomalous glass because plastic deformation is mostly through densification, in this study we used soda lime silica (SLS) glass which exhibits the deformation behavior of normal glass [23–25]. The topographic recovery of SLS was found to be between 99.94 and 99.97 % in the maximum contact pressure region; thus, the Hertzian contact was 'nearly-elastic', not fully elastic as previously assumed. The contacted surface region was slightly densified, and AFM-IR found corresponding changes in the vibrational spectral features. Surprisingly, the region outside the direct physical contact, which was elastically deformed along with the contacted region and fully recovered after unloading of the indenter, also showed a spectral shift that could be attributed to subsurface structural changes. Moreover, the top few nanometers of the physically-contacted surface region showed additional structural modification that rendered it more susceptible to base-catalyzed hydrolysis. This secondary damage mode was caused by interfacial friction, and its depth was much shallower than the principal stress fields generated by the Hertzian indentation.

2. Experimental method

2.1. Sample preparation and Hertzian indentation

Float glass panels (3.9 mm thick), obtained from the PPG Industries Works #6 plant (now Vitro Architectural Glass), were used in this study. The bulk composition of the glass was reported elsewhere [26]. The tin-side versus the air-side of the float glass panels was identified by X-ray photoelectron spectroscopy, and only the air-sides were analyzed in this study. Prior to any mechanical tests and surface characterization, the float glass samples were subjected to thermal annealing followed by cleaning process involving rinsing with acetone and ethanol in a sonication bath, followed by water rinsing and UV-Ozone treatment. For Hertzian indentation, a custom-built system was used, which was equipped with both environment control capability and an acoustic sensor to detect crack initiation events (Fig. 1(a)). Details of the Hertzian indentation setup can be found elsewhere [27]. An example of an *in situ* contact image with the indenter, obtained using an inverted microscope, is shown in Fig. 1(b) [28]. The maximum and average contact pressures, as well as contact diameter and deformation depth, were calculated from Hertzian contact mechanics [29]. An extended Hertzian theory[29] was also utilized to estimate the applicability of Hertzian theory on the current contact geometry. In the calculation, a 200 nm thick layer with an altered elastic modulus (±10 % of the elastic modulus of SLS glass) on

Table 1
Maximum and average contact pressure, contact diameter, and deformation depth of SLS indented with a WC ball (radius = 1 mm). The values are based on Hertzian theory [29]. The Vickers hardness and elastic modulus of SLS are also shown [26,32].

Applied load (N)	Hertzian contact pressure (GPa)		Contact diameter (μm)	Deformation depth (μm)
	Maximum	Average		
30	3.0	2.0	137	4.7
70	4.0	2.7	182	8.3
135	5.0	3.3	227	13
232	6.0	4.0	271	18.5

Vickers hardness = 5.8 GPa, Elastic modulus = 73 GPa.

top of the bulk SLS glass was assumed based on our previous work [30,31]. The results in Tables S1–3 demonstrated that the presence of a 200 nm thick top layer has negligible impact on the contact diameter, contact pressure, and deformation depth. Calculated results for a few representative load conditions are shown in Table 1, along with the reported values of Vickers hardness and elastic modulus of SLS [26,32]. Fig. 1(c) illustrates the topography of SLS surface deformed at a 40 N load, as calculated from Hertzian contact mechanics [33].

The indent tip was a 2-mm-diameter tungsten carbide (WC) sphere (ISO grade 3 with average roughness 10 nm). The load ramp rate for all the indentation testing was approximately 2 N/s. The crack initiation load (CIL) measurement was carried out with pristine samples and with the samples that were pre-indented with a pre-set load of 25 N or 100 N, which corresponded to the maximum Hertzian contact pressure of 2.8 or 4.5 GPa, respectively. The pre-indentation was done prior to the CIL measurement at the same indentation position. In brief, the sample was indented to the pre-set load, and the indenter was fully retracted. Then at the same location, the CIL measurement was done by ramping up the load at 2 N/s until a crack was detected by the acoustic sensor. All indentation tests were done in dry nitrogen environments (dew point <-30 °C). In order to produce control samples subjected to interfacial friction, the sample was contacted with the Hertzian indenter with an applied load of 3.5–5 GPa in paraffin oil and displaced laterally at a sliding speed of 0.1 mm/s. The topography and spherical depression of SLS glass surface were measured using an optical profilometer (Zygo NexView 3D optical profilometer) after the indentation. The residual depth of a spherical depression was determined from the local minimum height of the topography near spherical depression. Whenever crack appeared and a distinct roughness showed up within the residual depression, a baseline of the untouched surface was recorded at least 1000 μm away from the center of the depression. The residual depression was calculated by comparing the local minimum height of the topography near the spherical depression to the height of the baseline.

2.2. Photothermal AFM-IR and Raman spectroscopy measurements

The photothermal AFM-IR analysis was conducted using a Bruker IconIR system with a gold-coated PR-U-CnIR probe (spring constant = 0.2 N/m; resonant frequency = 13 kHz) in contact and surface-sensitive modes. The IR laser beam incidence angle was 72° (±8° based on the instrument specification). In the contact mode, the IR laser beam was modulated at the contact resonance frequency of 213.8 kHz and the signal was detected at the same frequency. In the surface-sensitive mode [34,35], the AFM probe was in contact with the surface in a force-modulation mode with a modulation frequency of 1823.9 kHz and the height change signal was detected at 413.7 kHz (which was close to the second harmonic of the contact resonance), while the IR laser repetition rate was adjusted automatically to the difference of the force modulation and detection frequencies (i.e., 1410.2 kHz). The probe depth of the contact mode was estimated to be >1 μm at the maximum peak position of the Si—O stretch mode based on the complex refractive

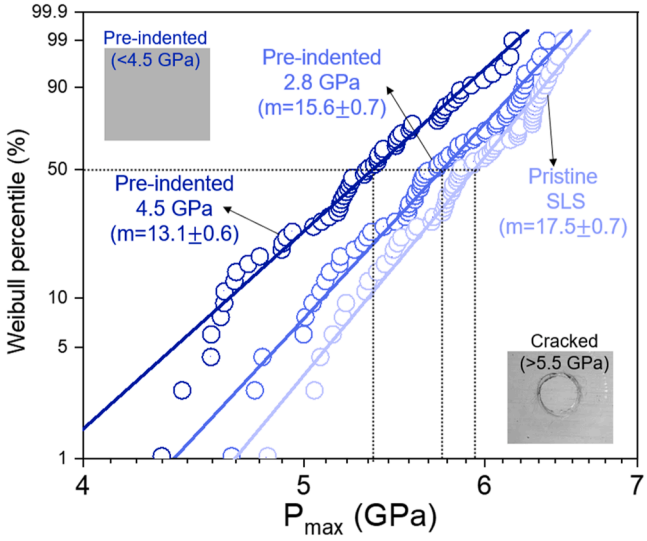

Fig. 2. Weibull plot of crack initiation load of pristine SLS glass (3.9 mm thick) and the surface contacted with the Hertzian indenter up to 2.8 GPa or 4.5 GPa maximum contact stress.

index of SLS and the previous theoretical calculation of the subsurface temperature rise upon irradiation of the sample with 100 ns IR pulse [16]. The probe depth of the surface-sensitive mode was estimated to be ~150 nm based on a calibration experiment performed with a polymer film on the same SLS glass (see Fig. S1 in the Supporting Information).

In addition, confocal Raman spectroscopy was performed for a selected SLS sample set using a Horiba LabRam system equipped with a monochromatic 229 nm laser and a 100× objective lens with a numerical aperture (NA) of 0.9. The data acquisition time was 180 s, and the laser power was set at 8 mW. Based on the excitation laser wavelength and the NA of the objective lens, the probe depth was estimated to be ~200 nm [36].

2.3. Aqueous corrosion test

The corrosion solutions (0.2 M NaOH) were prepared by mixing 300 g of ASTM Type 1 DI Water (LabChem Inc) with 5 g of a 50 wt.% solution of sodium hydroxide in water (Acros Ogranics) in a pre-cleaned 500 mL perfluoroalkoxy (PFA) jar (Savillex Corporation) containing a permeable Teflon sample holder [8]. The solution was then allowed 24 h to reach the target temperature, either in a fume hood with the temperature monitored by a thermometer (20 °C) or in an oven (Fisherbrand) maintained at the target temperature (90 °C). The cleaned and indented SLS samples were then lowered into the pre-heated solution on top of the Teflon sample holder, to allow for complete exposure of the sample to the solution. The containers were then returned to their isothermal condition (20 °C or 90 °C) for 2 h, after which the SLS samples were removed, rinsed with DI water, and blow-dried with nitrogen gas to remove excess water. Three-dimensional scans of the indents before and after corrosion and annealing were collected using an optical profilometer (Zygo NexView 3D optical profilometer). Data processing was performed with the Gwyddion software [37]. The height of never-touched flat region was offset to zero, and a low-pass gaussian filter (filter length = 2.3 nm) was applied to filter out noise at the sub-nanometer scale.

A control experiment was designed to verify if preferential corrosion occurs on the previously-indented glass surface after being subjected to a post-indentation annealing cycle. For this experiment, the glass was annealed at 520 °C. The temperature was gradually increased from 20 °C to 520 °C over a period of 1 hour, after which it was held at 520 °C for 2 h. Subsequently, the glass was cooled down slowly from 520 °C to 20 °C over a period of 16 h.

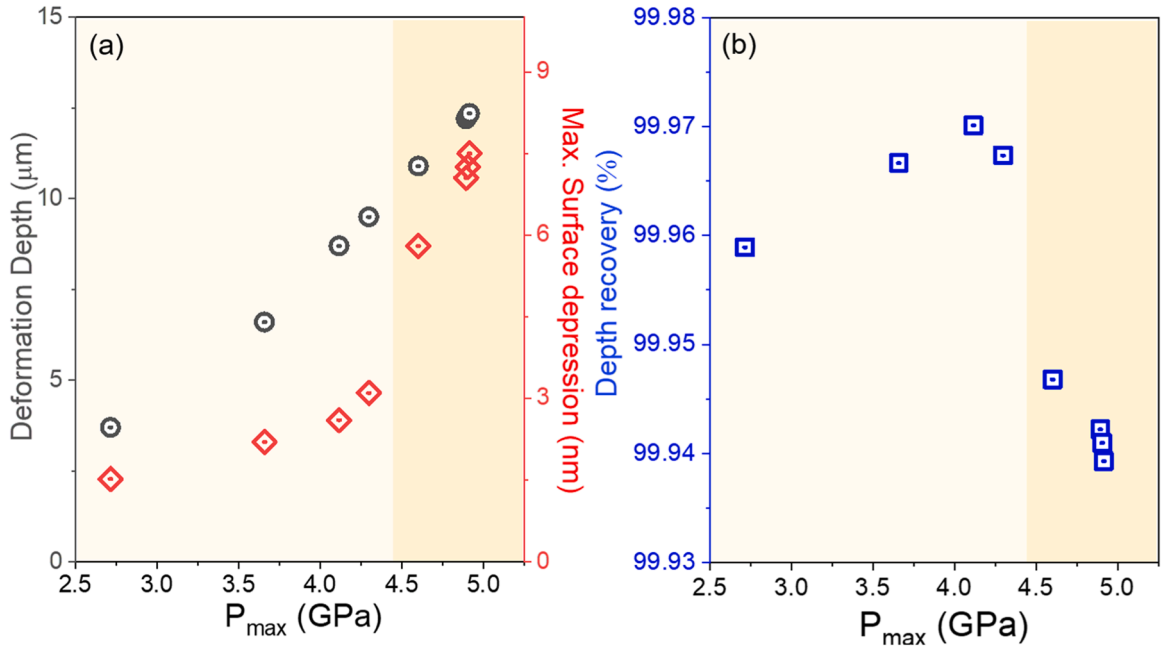

Fig. 3. (a) Deformation depth, maximum surface depression, and (b) depth recovery of SLS as a function of maximum pressure exerted on SLS surface upon indentation.

3. Results and discussion

3.1. Invisible defects weakening glass strength

When a foreign object come into physical contact with a glass, they can create surface defects that weaken the mechanical strength and chemical durability of the glass [6–10]. These surface defects can be manifest as plastic deformation [8,38,39] or surface cracking [40,41]. A control experiment was conducted to demonstrate that optically-invisible damage can also be made after nearly-elastic contact, which can weaken the apparent load to failure of glass. The SLS glass surface was pre-indented with a load low enough that no visual damage was observed under the optical microscope (inset image in the top left corner of Fig. 2, note that the inspection was done using a 20× objective, bright-field, transmitted-light microscope) and the same location was indented again until cracking was initiated (inset image in the bottom right corner of Fig. 2). Fig. 2 compares the Weibull plots of CIL measured for the pristine sample and the samples pre-indented at a maximum contact pressure of 2.8 and 4.5 GPa. The CIL at 50 % failure decreased from 5.94 GPa for the pristine surface to 5.78 GPa for the 2.8 GPa pre-load surface, and down to 5.32 GPa for the 4.5 GPa pre-load surface. In the low load regime, the change in the slope of the Weibull plot may suggest the presence of a secondary damage mode, but its origin could not be determined unambiguously. When the entire data set was used for statistical analysis, the changes in the Weibull modulus (i.e., the spread of data) were found to be statistically significant [42]. The confidence level of the difference in Weibull modulus was <95 % between the pristine and the 2.8 GPa pre-loaded samples and >95 % between the pristine and 4.5 GPa pre-loaded samples [42]. To better understand the surface defects created by the pre-indent load which weakened the glass strength, we have analyzed the indentation regions with surface-sensitive vibrational spectroscopy.

3.2. Subsurface structural change in nearly-elastic contact region and fully-elastic periphery

First, we checked if the topography of the pre-indented region was fully recovered, which will determine if the pre-indentation step at a light load really meets the formal definition of 'elastic' contact. For these experiments, glass specimens were first indented in strategic locations until visible cone-cracks were generated that could be used as fiducial markings for location reference. A series of pre-indentation tests were then conducted at lower loads, at known distances from the fiducial cracks. In this way, we were able to locate the nominally-elastic-indented regions with sufficient precision, even though they could not be found visually under the optical microscope with the highest possible magnification. A few topographic line profiles of the pre-indented regions are shown in Fig. S2, as obtained by optical profilometry. After indenting at low loads, there were very small residual indentation marks left on the surface. As shown in Fig. 3(a), the depths of the indents were only on the order of a few nanometers. When the residual indentation depth was compared with the Hertzian deformation depth [29], the depth recovery was found to be more than 99.94 %. It is interesting to note that when the maximum contact pressure was below 4.5 GPa, the recovery was 99.96–99.97 %; but as the contact load increased further, the recovery was decreased to approximately 99.94 %. Conventionally, there are three deformation processes that can occur during indentation on glass: plastic flow, densification, and elastic deformation. It has been reported that all three processes can occur for sharp indentation on SLS glass; however, for blunt (spherical) indentation with low compressive loading in elastic regime, it is not surprising that elastic deformation is the most dominating deformation process in the current study.

Comparing the residual indent diameter with the calculated Hertzian contact diameter, the plastically-deformed region was confined to the direct contact area. In other words, the region outside the contact which had no direct contact with the indenter (Fig. 1(c)) is fully recovered. Upon thermal annealing at sub-glass transition temperature (520 °C, which corresponded to 90 % of the glass transition temperature) [8,43], the residual indent disappeared completely (Fig. S2). This indicated that the plastic deformation in the direct contact area was mostly due to densification, resulting in a deficit of 0.03–0.06 % from the full recovery. There was no pile-up around the pre-indent area which could be identified within the height resolution of our optical profilometer. Thus, there was minimal to no plastic flow occurred. In other words, it can be concluded that topography-wise, the direct contact area is nearly-elastically recovered, and the never-touched periphery area was fully elastically recovered.

The direct contact and periphery areas of pre-indented samples were

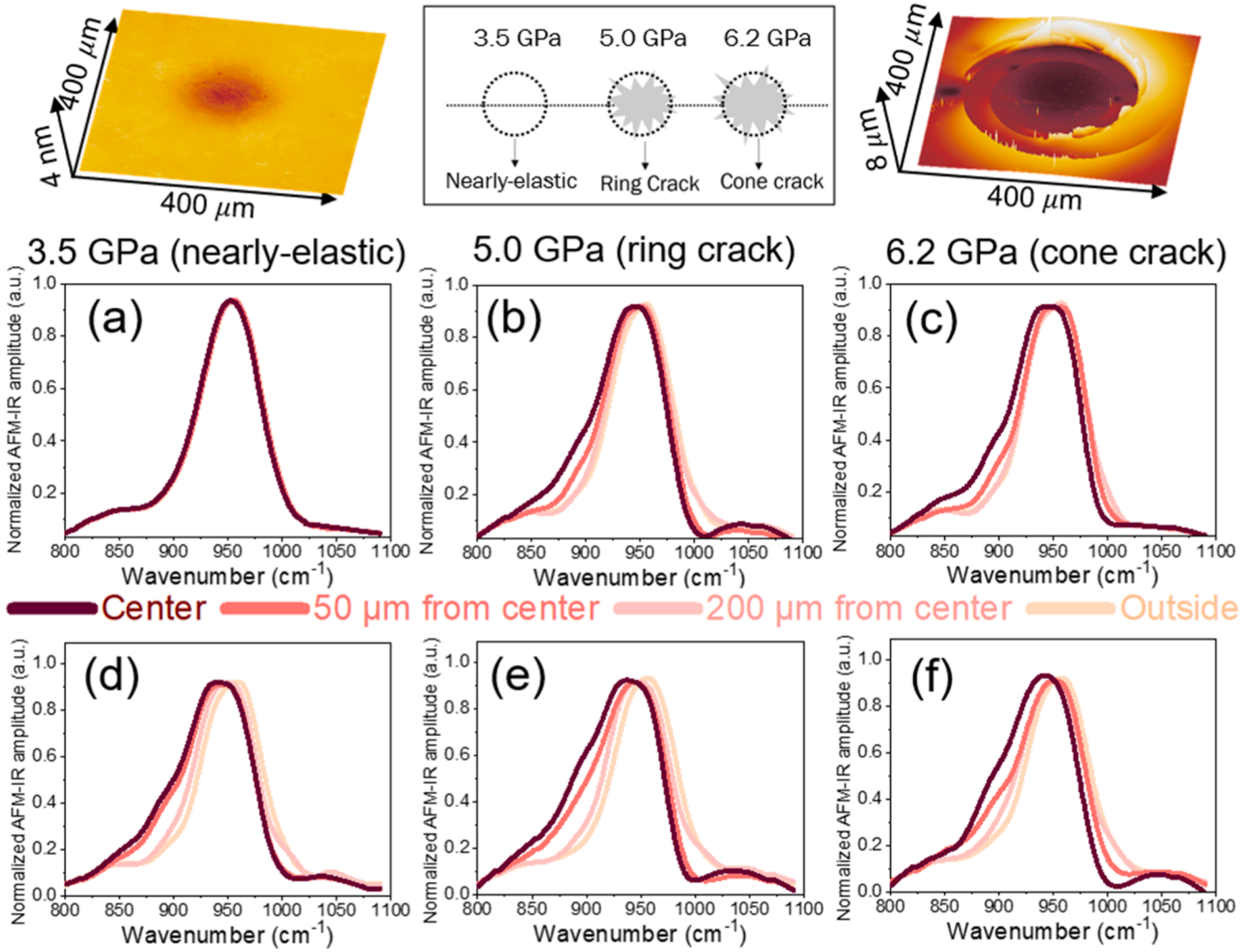

Fig. 4. AFM-IR spectra, collected with (a–c) contact mode (>1 μm probe depth) and (d–f) surface-sensitive mode (~150 nm probe depth), of SLS glass surfaces pre-indented with a tungsten carbide sphere up to (a, d) 3.5 GPa, (b, e) 5 GPa, and (c, f) 6.2 GPa. The spectra were collected at four locations per indent, which are color-coded as marked in the figure panel. The signal intensities were normalized to compare peak shape and position more easily.

analyzed with AFM-IR. Since the Hertzian deformation area (130–270 μm in diameter) was significantly larger than the scan range of AFM-IR (80 μm at maximum), full-scale imaging was not attempted. Instead, single-spot spectral analysis was conducted at the center of the direct contact area, 50 μm from the center, 200 μm from the center, and far away from the contact (reference point at which the pristine spectrum was collected). Fig. 4 displays the AFM-IR spectra of the SLS surfaces that were pre-indented with the maximum Hertzian contact pressure of 3.5 GPa, 5 GPa, and 6.2 GPa. Note that the maximum intensity position of the Si—O stretch band of SLS appears at ~960 cm^{-1} in AFM-IR, while it is ~1030 cm^{-1} in the optical extinction coefficient (k, imaginary part of complex refractive index) spectrum [44]. This is due to the convolution with optical reflection at the grazing incidence angle (72° from the surface normal axis) of the IR irradiation. Due to the same effect, the maximum intensity position of the Si—O stretch band appears at ~1200 cm^{-1} in the specular-reflection infrared spectrum (SR-IR) if the IR incidence angle is 70° [45].

In the locations where cracks were made (illustrated with gray shading on top of Fig. 4), both the contact mode (Fig. 4(b) and (c)) and surface-sensitive mode (Fig. 4(e) and (f)) detected evident changes in the Si—O stretch spectrum. This means that the subsurface region affected by indentation extends quite deep at this high load condition (maximum Hertzian contact pressure = 5.0 and 6.2 GPa). The peak position of the center region spectrum was slightly red-shifted, and the lower wavenumber region of the peak was significantly enhanced compared to the outside region (at least 5 mm away from contact region). Although it was difficult to quantify, the overall spectral changes were larger in the surface-sensitive mode (~150 nm probe depth) spectra than the contact mode spectra (>1 μm probe depth). In the location pre-indented at 3.5 GPa without cracking, the contact mode spectra (Fig. 4(a)) show no discernable difference between the center and periphery regions. However, the spectra collected with the surface-sensitive mode (Fig. 4 (d)) exhibited evident differences between the center and outside regions.

The spectral changes could be attributed to subsurface structural changes. If densification of the SLS glass occurs in a similar mode observed previously in silica and sodium silicate glasses [46,47], the red-shift of the Si—O stretching band can be attributed to the elongation of Si—O bonds. Similar red-shift of the Si—O stretching band was also observed with scattering-based nano-FTIR [6] in the periphery of the fused quartz densified indentation region. However, the data of nano-FTIR and AFM-IR cannot be directly correlated and compared due to differences in detection of material responses upon IR absorption [6, 16]. To address this, we have synthesized a hypothetical refractive index for the densified SLS glass based on the empirical correlation found in the silica and sodium silicate glasses and simulated the transient temperature profile, $\Delta T(\omega)$, of the densified SLS glass induced by the IR laser pulse irradiation (Fig. S3) [16]. The simulated transient temperature

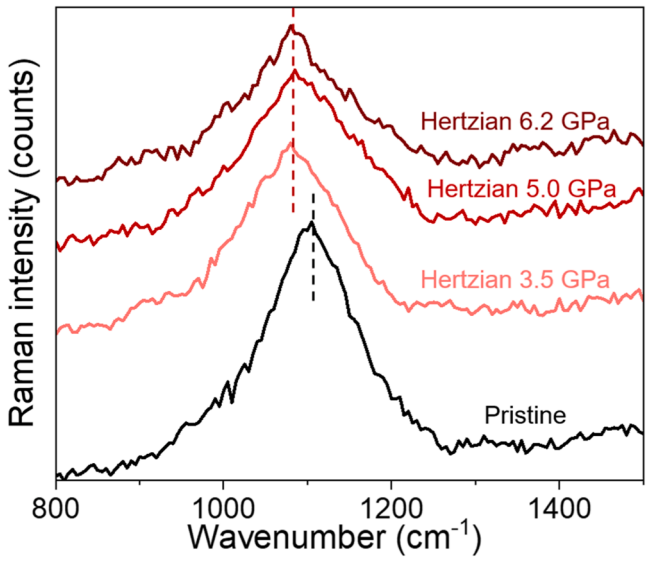

Fig. 5. Confocal Raman spectra of the SLS surfaces preloaded with Hertzian indentation.

change showed a red-shift of the Si—O stretch band in the $\Delta T(\omega)$ spectrum, which was consistent with the trend observed in experimental AFM-IR data (Fig. 4). Similar redshift of Si—O—Si stretching band has been reported previously, where indentation on SLS glass was reported to cause plastic dilatation that weakened the yield strength under tensile stress [48].

To confirm the subsurface densification of the direct contact region, we attempted to detect a spectral shift in the Si—O—Si bending mode region using Raman spectroscopy [49–51]. Assuming that the depth of the densified region is very shallow based on the lack of spectral changes in the contact mode AFM-IR of the 3.5 GPa indentation case (Fig. 4(a)), we employed the 229 nm excitation laser to ensure that the confocal Raman probe depth is ~200 nm [36]. Unfortunately, the Si—O—Si bending region could not be probed due to the absorption of the Rayleigh scattering filter in the system. Nonetheless, confocal Raman analysis with 229 nm excitation also showed a red-shift of the Si—O stretch mode, as exhibited in Fig. 5, which confirms that the red-shift in the AFM-IR is indeed due to the red-shift in the *k*-spectrum.

In Fig. 4, it is important to note that the AFM-IR spectral features are altered even at the position 200 μm away from the center of the contact. This was the periphery area that was deformed along with the contact region, but had not actually been physically touched by the probe (see Fig. 1(c) and Table 1). Based on the spectral contrast between the contact and surface-sensitive mode spectra (Fig. 4(a) vs. (d)), the depth of subsurface structural change was estimated to be very shallow. This spectral change in the Si—O network vibration must be due to the tensile stress created during the Hertzian indentation. Fig. 6 shows the principal normal stresses (maximum and minimum stresses, σ_1 and σ_3, and hoop stress, σ_2) as well as the maximum principal shear stress (τ_{13}) [52,53]. Table 2 summarizes the principal stresses in the near-surface region calculated for the 3.5 GPa maximum Hertzian contact pressure. At 200 μm from the contact center, the surface region still experiences about 70 MPa of tensile and hoop stresses. The structural changes detected with the surface-sensitive AFM-IR in the never-touched and fully-elastic deformation region (Fig. 4(a)) must be caused by these stresses (Fig. 6 (a) and (b)). In the previous SR-IR study investigating the flexural stress effect, the never-touched SLS surface under a 46 MPa tensile stress exhibited a small red-shift in the Si—O stretch peak position, although it was much smaller than the compressive stress side [54]. In addition, the

Table 2
Principal stress in SLS calculated at a depth of 80 nm (=0.001 × *a*) for the maximum Hertzian contact pressure of 3.5 GPa applied with a WC sphere with a radius of 1 mm. Here, the Hertzian contact radius (*a*) is 80 μm. For the principal normal stress, the negative sign means compressive stress and the positive sign means tensile stress [52,53].

Distance from the center	80 nm	80 μm	200 μm
σ_1	−1.68 GPa	+330 MPa	+70 MPa
σ_2	−1.68 GPa	−460 MPa	−70 MPa
σ_3	−2.33 GPa	−410 MPa	0
τ_{13}	330 MPa	190 MPa	30 MPa

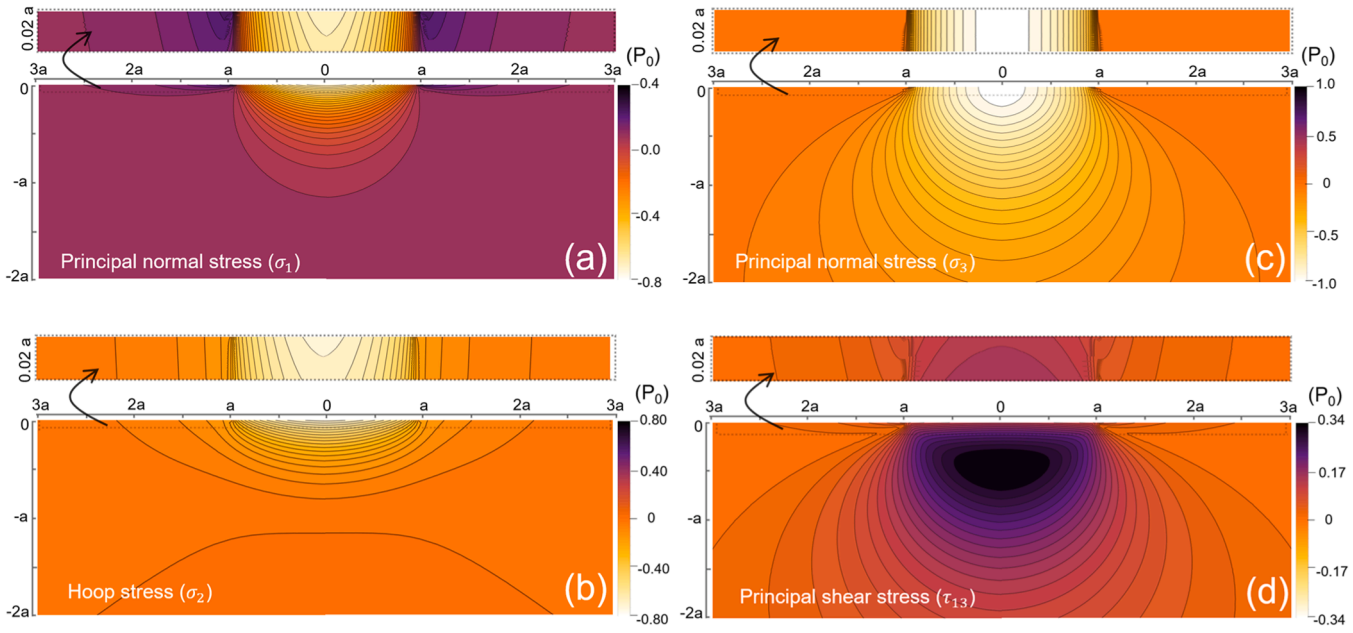

Fig. 6. Theoretically calculated Hertzian stress fields in the SLS glass [52,53]: (a–c) principal normal stresses where σ_1 and σ_3 are the maximum and minimum stress, respectively, and σ_2 is the hoop stress, and (d) maximum principal shear stress (τ_{13}). In the plot, the lateral length and depth scale with the Hertzian contact radius (*a* = half of the contact diameter shown in Table 1) and the stress (color map) scales with the average Hertzian pressure (shown in Table 1). In each panel, stress field of the top skin region (within 0.02 × *a* from the surface) is shown above the main plot covering the depth up to 2*a*.

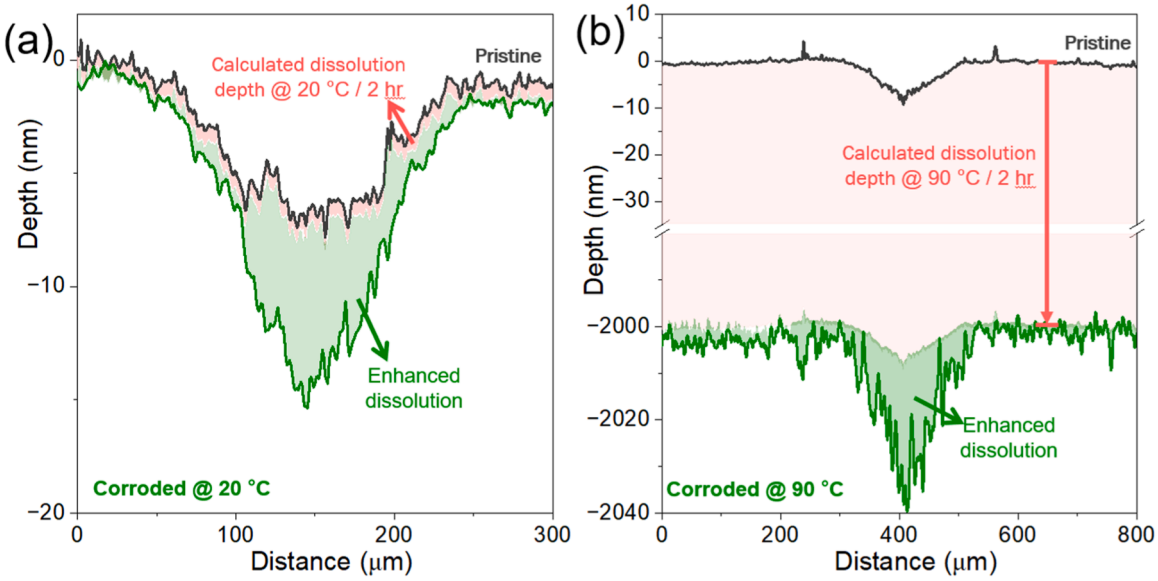

Fig. 7. Topographic line profiles of SLS glass surfaces indented with 5 GPa loading, before versus after corrosion at pH~13 for 2 h at (a) 20 °C and (b) 90 °C. The pink shaded area represents ordinary dissolution in basic solution estimated from the hydrolysis rate of SLS [56], while the green shaded area represents the enhanced dissolution due to the subsurface damage made during the Hertzian indentation. (For interpretation of the references to color in this figure legend, the reader is referred to the web version of this article.)

subsurface structural change may not be limited to changes in bond length distribution. In another molecular dynamic (MD) simulation study, Si—O—Si bond-breaking (cavity in SLS glass network) was observed under 5 GPa of tensile stress [55]. Such formation of cavity in the glass network can be relevant to the weakening of the glass after nearly-elastic contact. The full interpretation of the spectral changes observed in this untouched and fully-elastic deformation region of the SLS glass is currently difficult to make and needs further study.

3.3. Subsurface damage due to interfacial shear during physical contact

While spectroscopic analysis can nondestructively probe subsurface structural changes, as demonstrated in Figs. 4 and 5, chemical etching can also be used to reveal or selectively remove the damaged region, as it will be more susceptible to chemical attack. The pre-indented SLS samples were treated with a pH~13 NaOH solution for 2 h at either 20 °C or 90 °C. The topographic images of SLS glass surfaces before and after aqueous corrosion were captured by optical profilometry and compared to deduce the depth of the enhanced corrosion of the damaged region. The nominal corrosion rate of SLS glass was estimated to be 0.33 nm/h at 20 °C, 0.1 μm/h at 70 °C, and ~1 μm/h at 90 °C [56]. As shown in Fig. 7, the etching depth could be divided into 'normal' and 'enhanced' corrosion regions. The results showed that the indented regions exhibited a disproportionate increase in corrosion depth when exposed to the basic solution.

The width of the enhanced corrosion area did not increase from the initial residual imprint which was the same as the Hertzian contact diameter (Fig. 1(c) and Table 1). This denoted that the subsurface damage preferentially etched at pH 13 corresponded to the region in direct physical contact with the indenter tip. The periphery of the contact region did not show any detectable enhancement in chemical etching, which indicated that the subsurface structural changes made by the σ_1 tensile stress outside the direct physical contact area (for example, the 200 mm region in Fig. 4(a)) did not lead to detectable enhancement of corrosion rate in the basic solution.

The maximum depth of preferential etching at pH 13 at 90° for 2 h

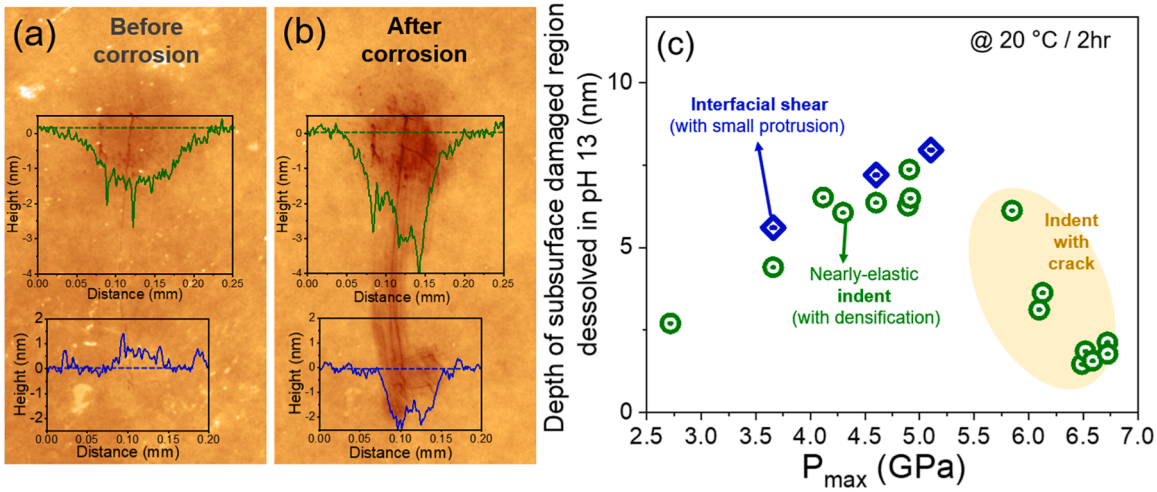

Fig. 8. Topography of indentation mark (a) before and (b) after corrosion at pH 13. (c) Depth of subsurface damaged region dissolved at pH 13 for 2 h as a function of maximum pressure exerted on SLS surface upon indentation. Another example is shown in Fig. S4.

was about 30 nm (Figs. 7(b) and S4). Since the total dissolution depth in this condition (~2 μm) was much larger than this value, it can be said that the depth of chemically-etchable subsurface damage made during the Hertzian indentation was only approximately 30 nm or less. Then, what could be the origin for this very shallow subsurface damage? One may question if that is due to the principal shear stress (τ_{13}) generated during the Hertzian indentation (Fig. 6(d)). We believe this is very unlikely. First, the calculation with Hertzian contact mechanics predicted that τ_{13} increases from 460 MPa right at the surface to its maximum (1.1 GPa) at ~50 μm from the surface when the applied maximum Hertzian contact pressure is 5 GPa. But the preferential etching stopped at ~30 nm (Fig. 7(b)). Also, it should be noted that τ_{13} is a static stress and it does not mean a real shear.

Ruling out the effect of the principal shear stress, we hypothesized that the interfacial shear (i.e., friction) is the main cause for the subsurface damage associated with the accelerated chemical etching [7,8,57,58]. In a previous study investigating the wear behavior of the SLS surface, it was found that the friction-tested track with no visual wear can be preferentially etched by hydrothermal treatment at >150 °C [7]. In the current study, we sometimes found that the never-touched periphery of the indent mark revealed a thin and shallow etch track in the region that did not show any obvious damage before etching (Fig. 8(b)). The presence of such a line was not obvious before etching in pH 13 (Fig. 8(a)). But, when the profilometry image of the pre-etch surface was re-analyzed, a small protrusion in the region etched by pH 13 was always observed (see blue line profile in Fig. 8(a)). The protrusion of the surface topography could mean that the subsurface region is less dense, which may be the reason that the damaged region becomes more vulnerable to hydrolysis at pH 13. A similar behavior was also observed in nano-scale friction experiments [59–61]. We speculated that the indenter tip might have slipped during the unloading due to the instability or asymmetry of the load structure of our Hertzian indentation system; such a slip might have occurred when the elastic recovery force of the load structure became larger than the static friction of the contact point. A similar phenomenon was observed previously at the end of a nanoscratch mark [6].

To further corroborate this hypothesis, we have intentionally displaced the indenter at its maximum applied load and subjected the sample to the aqueous corrosion at pH~13 at 25 °C for 2 h. The sliding was performed in paraffin oil to prevent any physical scratching. The data shown in Fig. S5 confirmed that the slip of the tip indeed created the chemically-etchable subsurface damage. The etch depth observed in the control experiment closely matched with the preferential etch depth observed for the Hertzian indentation mark (Fig. 8(c)).

It is also interesting to note that the preferential etch depth decreased when the cone crack was formed during the Hertzian indentation (highlighted with a yellow background in Fig. 8(b)). Once the crack was formed, the glass surface remained suppressed (Fig. S2(b)). Then, when the slip occurred during the unloading step, the actual friction at the interface between the tip and the glass surface would have been smaller. Thus, the subsurface damage due to friction could have been less. This further corroborated the hypothesis that the chemically-etchable subsurface damage is caused by interfacial friction by the indenter, not by the compressive or shear stresses created during the indentation in ideal condition. The preferential dissolution behavior disappeared if the sample was annealed at a sub-T_g temperature (Fig. S2(a)). This indicates that annealing reverted all subsurface damage caused by the compressive stress during the indentation along the surface-normal direction and frictional stress due to the tip along the surface-parallel direction.

4. Conclusion

We have identified three modes of subsurface changes when the glass is physically touched with a foreign object, which is graphically illustrated in Fig. 9. The first is structural changes in the glass network due to compressive stress during the indentation along the surface normal direction. The compressive stress in the direct physical contact region leads to a small degree of subsurface densification even though the maximum contact pressure is far below the hardness of the glass, so the topographic alteration of the surface is extremely small and invisible under a typical optical microscope at the highest magnification. The second mode is structural changes due to tensile stress in the periphery of the indentation contact even though the glass surface had not experienced any direct contact with the foreign object and fully recovered topography-wise. The third is the damage caused by interfacial friction; the friction-induced damage region is very shallow (<30 nm from the surface) and becomes more vulnerable to base-catalyzed hydrolysis.

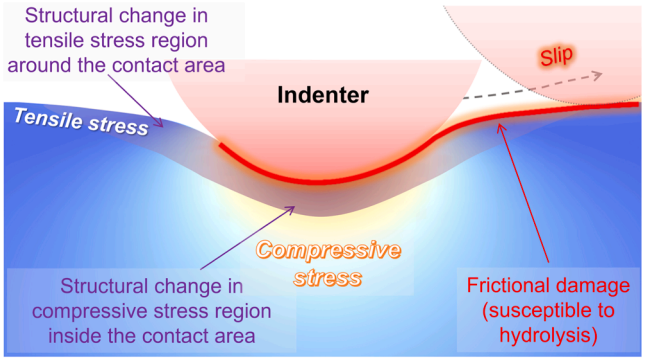

Fig. 9. Schematic illustration of stresses generated during the Hertzian indentation and subsurface structural changes revealed by surface-sensitive vibrational spectroscopy and chemical etching.

Declaration of Competing Interest

The authors declare the following financial interests/personal relationships which may be considered as potential competing interests:

This work was supported by Corning Incorporated and the National Science Foundation (grant no. DMR-2011410). ANZ participated in this research with the support from National Aeronautics and Space Administration under Grant no. 80NSSC20M0097 issued through the Pennsylvania Space Grant Consortium.

Acknowledgments

This work was supported by Corning Incorporated and the National Science Foundation (grant no. DMR-2011410). ANZ participated in this research with the support from National Aeronautics and Space Administration under Grant no. 80NSSC20M0097 issued through the Pennsylvania Space Grant Consortium. The authors acknowledged Dr. Maxwell Wetherington at the Penn State Materials Characterization Lab for technical assistance of AFM-IR. The authors also acknowledged Amber Tremper-Leigh from Corning Incorporated for reviewing the document and providing useful feedback.

Supplementary materials

Supplementary material associated with this article can be found, in the online version, at doi:10.1016/j.actamat.2023.119571.

References

[1] F. Kotz, K. Arnold, W. Bauer, D. Schild, N. Keller, K. Sachsenheimer, T.M. Nargang, C. Richter, D. Helmer, B.E. Rapp, Three-dimensional printing of transparent fused silica glass, Nature 544 (7650) (2017) 337–339.
[2] L. Wondraczek, J.C. Mauro, J. Eckert, U. Kuhn, J. Horbach, J. Deubener, T. Rouxel, Towards ultrastrong glasses, Adv. Mater. 23 (39) (2011) 4578–4586.
[3] X. Lu, Z. Wang, X. Yang, X. Xu, L. Zhang, N. Zhao, J. Xu, Antifogging and antireflective silica film and its application on solar modules, Surf. Coat. Technol. 206 (6) (2011) 1490–1494.

[4] X. Yu, T.J. Marks, A. Facchetti, Metal oxides for optoelectronic applications, Nat. Mater. 15 (4) (2016) 383–396.
[5] K. Nomura, H. Ohta, A. Takagi, T. Kamiya, M. Hirano, H. Hosono, Room-temperature fabrication of transparent flexible thin-film transistors using amorphous oxide semiconductors, Nature 432 (7016) (2004) 488–492.
[6] H. He, Z. Chen, Y.-T. Lin, S.H. Hahn, J. Yu, A.C. van Duin, T.D. Gokus, S.V. Rotkin, S.H. Kim, Subsurface structural change of silica upon nanoscale physical contact: chemical plasticity beyond topographic elasticity, Acta Mater. 208 (2021), 116694.
[7] J. Luo, H. Huynh, C.G. Pantano, S.H. Kim, Hydrothermal reactions of soda lime silica glass—Revealing subsurface damage and alteration of mechanical properties and chemical structure of glass surfaces, J. Non-Cryst. 452 (2016) 93–101.
[8] H. He, S.H. Hahn, J. Yu, Q. Qiao, A.C. van Duin, S.H. Kim, Friction-induced subsurface densification of glass at contact stress far below indentation damage threshold, Acta Mater. 189 (2020) 166–173.
[9] O. Benzine, S. Bruns, Z. Pan, K. Durst, L. Wondraczek, Local deformation of glasses is mediated by rigidity fluctuation on nanometer scale, Adv. Sci. 5 (10) (2018), 1800916.
[10] G. Brambilla, D.N. Payne, The ultimate strength of glass silica nanowires, Nano Lett. 9 (2) (2009) 831–835.
[11] A. Llordés, G. Garcia, J. Gazquez, D.J. Milliron, Tunable near-infrared and visible-light transmittance in nanocrystal-in-glass composites, Nature 500 (7462) (2013) 323–326.
[12] S.K. Lee, P.J. Eng, H.-K. Mao, Y. Meng, M. Newville, M.Y. Hu, J. Shu, Probing of bonding changes in B_2O_3 glasses at high pressure with inelastic X-ray scattering, Nat. Mater. 4 (11) (2005) 851–854.
[13] T. Geisler, L. Dohmen, C. Lenting, M.B. Fritzsche, Real-time in situ observations of reaction and transport phenomena during silicate glass corrosion by fluid-cell Raman spectroscopy, Nat. Mater. 18 (4) (2019) 342–348.
[14] M. Liu, A.J. Sternbach, M. Wagner, T.V. Slusar, T. Kong, S.L. Bud'ko, S. Kittiwatanakul, M. Qazilbash, A. McLeod, Z. Fei, Phase transition in bulk single crystals and thin films of VO_2 by nanoscale infrared spectroscopy and imaging, Phys. Rev. B 91 (24) (2015), 245155.
[15] A. Dazzi, C.B. Prater, AFM-IR: technology and applications in nanoscale infrared spectroscopy and chemical imaging, Chem. Rev. 117 (7) (2017) 5146–5173.
[16] Y.-T. Lin, H. He, H. Kaya, H. Liu, D. Ngo, N.J. Smith, J. Banerjee, A. Borhan, S. H. Kim, Photothermal atomic force microscopy coupled with infrared spectroscopy (AFM-IR) analysis of high extinction coefficient materials: a case study with silica and silicate glasses, Anal. Chem. 94 (13) (2022) 5231–5239.
[17] Y.-C. Lan, S. Kamal, C.-C. Lin, Y.-H. Liu, K.-L. Lu, Ultra-thin Zr-MOF/PVA/Melamine composites with remarkable sound attenuation effects, Microporous Mesoporous Mater. 360 (2023), 112668.
[18] D.V. Benedis, A. Dazzi, M. Rivallan, G.D. Pirngruber, Surface heterogeneity in amorphous silica nanoparticles evidenced from tapping AFM–IR nanospectroscopy, Anal. Chem. 95 (2) (2022) 1505–1512.
[19] H.T. Smyth, Elastic properties of glasses, J. Am. Ceram. Soc. 42 (6) (1959) 276–279.
[20] F. Leonforte, A. Tanguy, J. Wittmer, J.-L. Barrat, Inhomogeneous elastic response of silica glass, Phys. Rev. Lett. 97 (5) (2006), 055501.
[21] J. Kjeldsen, M.M. Smedskjaer, M. Potuzak, Y. Yue, Role of elastic deformation in determining the mixed alkaline earth effect of hardness in silicate glasses, J. Appl. Phys. 117 (3) (2015), 034903.
[22] A.K. Varshneya, G. Macrelli, S. Yoshida, S.H. Kim, A.L. Ogrinc, J.C. Mauro, Indentation and abrasion in glass products: lessons learned and yet to be learned, Int. J. Appl. Glass Sci. 13 (3) (2022) 308–337.
[23] V.Le Houérou, J.-C. Sangleboeuf, T. Rouxel, Scratchability of soda-lime silica (SLS) glasses: dynamic fracture analysis. Key Engineering Materials, Trans Tech Publ, 2005, pp. 31–38.
[24] A. Koike, M. Tomozawa, Fictive temperature dependence of subcritical crack growth rate of normal glass and anomalous glass, J. Non-Cryst. 352 (52–54) (2006) 5522–5530.
[25] A. Arora, D. Marshall, B. Lawn, M. Swain, Indentation deformation/fracture of normal and anomalous glasses, J. Non-Cryst. 31 (3) (1979) 415–428.
[26] N. Sheth, A. Howzen, A. Campbell, S. Spengler, H. Liu, C.G. Pantano, S.H. Kim, Effects of tempering and heat strengthening on hardness, indentation fracture resistance, and wear of soda lime float glass, Int. J. Appl. Glass Sci. 10 (4) (2019) 431–440.
[27] J. Luo, Understanding Shear-Induced Hydrolysis Reactions on Soda Lime Silica Glass Surface, Ph.D. Thesis, 2018.
[28] N.D. Surdyka, C.G. Pantano, S.H. Kim, Environmental effects on initiation and propagation of surface defects on silicate glasses: scratch and fracture toughness study, Appl. Phys. A 116 (2) (2014) 519–528.
[29] S. Liu, A. Peyronnel, Q. Wang, L. Keer, An extension of the Hertz theory for three-dimensional coated bodies, Tribol. Lett. 18 (2005) 303–314.
[30] N. Sheth, D. Ngo, J. Banerjee, Y. Zhou, C.G. Pantano, S.H. Kim, Probing hydrogen-bonding interactions of water molecules adsorbed on silica, sodium calcium silicate, and calcium aluminosilicate glasses, J. Phys. Chem. C 122 (31) (2018) 17792–17801.
[31] N. Sheth, S.H. Hahn, D. Ngo, A. Howzen, R. Bermejo, A.C. van Duin, J.C. Mauro, C. G. Pantano, S.H. Kim, Influence of acid leaching surface treatment on indentation cracking of soda lime silicate glass, J. Non-Cryst. 543 (2020), 120144.
[32] H. Sawasato, S. Yoshida, T. Sugawara, Y. Miura, J. Matsuoka, Relaxation behaviors of Vickers indentations in soda-lime glass, J. Ceram. Soc. Jpn. 116 (1356) (2008) 864–868.
[33] T. Jacobs, A. Martini, Measuring and understanding contact area at the nanoscale: a review, Appl. Mech. Rev. 69 (6) (2017), 060802.
[34] J. Mathurin, A. Deniset-Besseau, D. Bazin, E. Dartois, M. Wagner, A. Dazzi, Photothermal AFM-IR spectroscopy and imaging: status, challenges, and trends, J. Appl. Phys. 131 (1) (2022), 010901.
[35] J. Mathurin, A. Deniset-Besseau, A. Dazzi, Advanced infrared nanospectroscopy using photothermal induced resonance technique, AFMIR: new approach using tapping mode, Acta Phys. Pol. A. 137 (1) (2020).
[36] N.J. Everall, Confocal Raman microscopy: performance, pitfalls, and best practice, Appl. Spectrosc. 63 (9) (2009) 245A–262A.
[37] D. Nečas, P. Klapetek, Gwyddion: an open-source software for SPM data analysis, Open Phys. 10 (1) (2012) 181–188.
[38] K. Li, Y. Shapiro, J. Li, Scratch test of soda-lime glass, Acta Mater. 46 (15) (1998) 5569–5578.
[39] S. Yoshida, H. Sawasato, T. Sugawara, Y. Miura, J. Matsuoka, Effects of indenter geometry on indentation-induced densification of soda-lime glass, J. Mater. Res. 25 (11) (2010) 2203–2211.
[40] S. Wiederhorn, L. Bolz, Stress corrosion and static fatigue of glass, J. Am. Ceram. Soc. 53 (10) (1970) 543–548.
[41] S.M. Wiederhorn, Influence of water vapor on crack propagation in soda-lime glass, J. Am. Ceram. Soc. 50 (8) (1967) 407–414.
[42] D. Hudak, M. Tiryakioğlu, On comparing the shape parameters of two Weibull distributions, Mater. Sci. Eng. A 528 (27) (2011) 8028–8030.
[43] T. Gross, Deformation and cracking behavior of glasses indented with diamond tips of various sharpness, J. Non-Cryst. 358 (24) (2012) 3445–3452.
[44] J. Luo, N.J. Smith, C.G. Pantano, S.H. Kim, Complex refractive index of silica, silicate, borosilicate, and boroaluminosilicate glasses—Analysis of glass network vibration modes with specular-reflection IR spectroscopy, J. Non-Cryst. 494 (2018) 94–103.
[45] H. Liu, H. Kaya, Y.T. Lin, A. Ogrinc, S.H. Kim, Vibrational spectroscopy analysis of silica and silicate glass networks, J. Am. Ceram. Soc. 105 (4) (2021) 2355–2384.
[46] H. Liu, S.H. Hahn, M. Ren, M. Thiruvillamalai, T.M. Gross, J. Du, A.C. van Duin, S. H. Kim, Searching for correlations between vibrational spectral features and structural parameters of silicate glass network, J. Am. Ceram. Soc. 103 (6) (2020) 3575–3589.
[47] J. Luo, Y. Zhou, C.G. Pantano, S.H. Kim, Correlation between IR peak position and bond parameter of silica glass: molecular dynamics study on fictive temperature (cooling rate) effect, J. Am. Ceram. Soc. 101 (12) (2018) 5419–5427.
[48] A. Koike, M. Tomozawa, IR investigation of density changes of silica glass and soda-lime silicate glass caused by microhardness indentation, J. Non-Cryst. 353 (24–25) (2007) 2318–2327.
[49] T. Deschamps, A. Kassir-Bodon, C. Sonneville, J. Margueritat, C. Martinet, D. De Ligny, A. Mermet, B. Champagnon, Permanent densification of compressed silica glass: a Raman-density calibration curve, J. Phys. Condens. Matter. 25 (2) (2012), 025402.
[50] A. Kassir-Bodon, T. Deschamps, C. Martinet, B. Champagnon, J. Teisseire, G. Kermouche, Raman mapping of the indentation-induced densification of a soda-lime-silicate glass, Int. J. Appl. Glass Sci. 3 (1) (2012) 29–35.
[51] M. Heili, B. Poumellec, E. Burov, C. Gonnet, C.Le Losq, D.R. Neuville, M. Lancry, The dependence of Raman defect bands in silica glasses on densification revisited, J. Mater. Sci. 51 (2016) 1659–1666.
[52] D. Louapre, K. Breder, Hertzian indentation stress field equations, Int. J. Appl. Ceram. Technol. 12 (5) (2015) 1071–1079.
[53] B.R. Lawn, Indentation of ceramics with spheres: a century after Hertz, J. Am. Ceram. Soc. 81 (8) (1998) 1977–1994.
[54] H. Liu, H. He, Z. Chen, S.H. Kim, Flexural stress effect on mechanical and mechanochemical properties of soda lime silicate glass surface, J. Am. Ceram. Soc. 105 (4) (2022) 2847–2857.
[55] S. Ito, T. Taniguchi, Effect of cooling rate on structure and mechanical behavior of glass by MD simulation, J. Non-Cryst. 349 (2004) 173–179.
[56] J.P. Guin, S.M. Wiederhorn, T. Fett, Crack-tip structure in soda–lime–silicate glass, J. Am. Ceram. Soc. 88 (3) (2005) 652–659.
[57] E. Silva, J. Li, D. Liao, S. Subramanian, T. Zhu, S. Yip, Atomic scale chemo-mechanics of silica: nano-rod deformation and water reaction, J. Comput. Aided Mol. Des. 13 (2006) 135–159.
[58] T.A. Michalske, B. Bunker, Slow fracture model based on strained silicate structures, J. Appl. Phys. 56 (10) (1984) 2686–2693.
[59] B. Yu, X. Li, H. Dong, Y. Chen, L. Qian, Z. Zhou, Towards a deeper understanding of the formation of friction-induced hillocks on monocrystalline silicon, J. Phys. D 45 (14) (2012), 145301.
[60] B. Yu, L. Qian, H. Dong, J. Yu, Z. Zhou, Friction-induced hillocks on monocrystalline silicon in atmosphere and in vacuum, Wear 268 (9–10) (2010) 1095–1102.
[61] B. Yu, H. Dong, L. Qian, Y. Chen, J. Yu, Z. Zhou, Friction-induced nanofabrication on monocrystalline silicon, Nanotechnol 20 (46) (2009), 465303.